Journal of
Materials Chemistry C

Accepted Manuscript

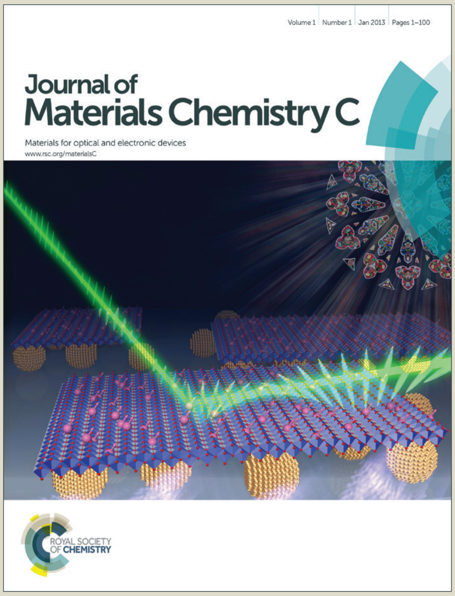

ROYAL SOCIETY
OF CHEMISTRY

www.rsc.org/materialsC

Journal Name

ARTICLE

Analysing the effect of the crystal structure on upconversion luminescence in Yb^{3+}, Er^{3+}-co-doped $NaYF_4$ nanomaterial

Received 00th January 20xx,
Accepted 00th January 20xx

DOI: 10.1039/x0xx00000x

www.rsc.org/

D. T. Klier[a]† and M. U. Kumke[a]†

$NaYF_4$:Yb:Er nanoparticles (UCNP) were synthesized under mild experimental conditions to obtain a pure cubic lattice. Upon annealing at different temperatures up to T_{an} = 700°C phase transitions to the hexagonal phase and back to the cubic phase were induced. The UCNP materials obtained for different T_{an} were characterized with respect to the lattice phase using standard XRD and Raman spectroscopy as well as steady state and time resolved upconversion luminescence. The standard techniques showed that for the annealing temperature range 300°C < T_{an} < 600°C the hexagonal lattice phase was dominant. For T_{an} < 300°C hardly any change in the lattice phase could be deduced, whereas for T_{an} > 600°C a back transfer to the α-phase was observed. Complementary, the luminescence upconversion properties of the annealed UCNP materials were characterized in steady state and time resolved luminescence measurements. Distinct differences in the upconversion luminescence intensity, the spectral intensity distribution and the luminescence decay kinetics were found for the cubic and hexagonal lattice phase, respectively, corroborating the results of the standard analytical techniques used. In laser power dependent measurements of the upconversion luminescence intensity it was found that the green (G1, G2) and red (R) emission of Er^{3+} showed different effects of T_{an} on the number of required photons reflecting the differences in the population routes of the different energy levels involved. Furthermore, the intensity ratio of G_{full}/R is highly efected by the laser power only when the β-phase is present, whereas the G1/G2 intensity ratio is only slightly effected regardless of the crystal phase. Moreover, based on the different upconversion luminescence kinetics characteristic for the cubic and hexagonal phase time-resolved area normalized emission spectra (TRANES) proved to be a very sensitive tool to monitor the phase transition between cubic and hexagonal phase. Based on the TRANES analysis it was possible to resolve the lattice phase transition in more detail for 200°C < T_{an} < 300°C, which was not possible with the standard techniques.

1. Introduction

Nanomaterials labeled with fluorescent dyes have been widely used in life-science applications and biological studies.[1-6] Typically, these labeling compounds are organic dyes, such as Alexa Fluor, fluorescein isothiocyanate (FITC), cyanine dyes (Cy3, Cy5 or Cy7) and rhodamin derivates.[7-9] Recently, semiconductor quantum dots have emerged as great potential candidates for life-science applications.[10-16] These conventional down conversion luminescence probes require light in the ultra violet or visible spectral range for excitation. Their main disadvantages are the background-related auto-fluorescence of biological samples due to the UV/Vis excitation wavelengths typically used, photobleaching of the probes, low light penetration depth in tissues like skin and possible damages to the biological matrix under investigation.[1,7,17]

Upconversion (UC) luminescent materials have attracted a great interest in recent years due to their outstanding photophysical properties and the resulting application potentials in various fields such as solid-state lasers, solar cells, color displays or life sciences.[18-27] Upconversion materials based on lanthanide-doped fluorides received a lot of attention owing to their high UC efficiency and photostability. Highly efficient UC materials among various fluoride based UC phosphors are β-phase $NaYF_4$ doped with Yb^{3+} and Er^{3+} or Yb^{3+} and Tm^{3+} as sensitizer-activator pair, respectively.[28-33] The luminescence properties of upconversion nanoparticles (UCNP) are dependent on a complex interplay between the different dopant ions on the one hand side and the host lattice on the other hand side.[8,9,34] Thus, the luminescence of these particles can be tuned by the crystal structure of the host lattice, the particle size, the ratio of the different lanthanides used as dopands, and the power density of the excitation light.[35] E.g., for $NaYF_4$ the host lattice geometry can be switched by annealing between the cubic (α) and the hexagonal (β) phase subsequently also tuning the UC properties of the materials.[20,36-39]

In the present study, the UCNP were synthesized under mild reaction conditions ($T_{synthesis}$ = 160°C) in order to obtain a pure cubic (α) phase host lattice. Subsequently, in order to investigate the influence of the crystal phase on the upconversion luminescence properties different annealing temperatures (T_{an}) were applied to induce a phase transition in the material. The alterations in the photophysical properties of

---

[a] *University of Potsdam, Department of Chemistry (Physical Chemistry), Karl-Liebknecht-Str. 24-25, 14476 Potsdam, Germany.*

†*:These authors equally contributed to this study.*

Electronic Supplementary Information (ESI) available: TEM image of $UCNP_{400}$ is shown as well as further detailed XRD diffractograms of $UCNP_x$ and crystallite size out of the *Debye-Scherrer* calculation. See DOI: 10.1039/x0xx00000x the UCNP materials obtained for different T_{an} were monitored using steady state and time-resolved luminescence techniques. Time-resolved area-normalized emission spectra (TRANES) can often be useful method to illustrate the overall dynamic, especially to identify at least two emissive states.[40-45] Based on the luminescence data the interplay of the population routes of sensitizer and activator electronic states involved in the different luminescence upconversion processes were analyzed in order to increase the understanding of the UCNP photophysics. The detailed knowledge of it on a molecular level provides the basis for UCNP material synthesis tailored for the specific needs of applications they are going to be used such as multiplexing applications like temperature sensing or in vivo imaging. The upconversion luminescence data are complemented by Raman, SEM and XRD measurements to determine the size and the crystal phase of the UCNP investigated and to underline the power of luminescence techniques in the structural characterization of such materials.

2. Experimental

2.1 Materials

All rare earth oxides RE_2O_3 (RE: Y, Yb and Er) were purchased from Chem Pur Feinchemikalien and Forschungsbedarf GmbH. Sodium fluoride (NH_4F, 99%) was purchased from Sigma Aldrich. Nitric acid solution (HNO_3, 65%), sodium chlorid and ethanol (99.5%) was purchased from Carl Roth. Polyvinylpyrrolindone (PVP 40). In the experiments double distilled water was used. In the synthesis all chemical reagents were used as received.

2.2 Synthesis of NaYF4:Yb3+:Er3+ UCNP

The UCNPs were synthesized according to a previously reported procedure in which a well-known hydrothermal method with PVP 40 as a capping agent was applied.[1,29,46] The rare earth nitrates ($RE(NO_3)_3$) were prepared from the corresponding oxides in stoichiometric amounts of Y_2O_3 (3.9 mmol), Yb_2O_3 (1.0 mmol) and Er_2O_3 (0.1 mmol) dissolved in nitric acid (200 mL, 10%) according to the literature method.[47] Typically, the obtained $RE(NO_3)_3$, was dissolved in 200 mL ethylene glycol and was treated with a mixture of NaCl (20 mmol) and 8.9 g PVP 40 (solution A). NH_4F (80 mmol) was dissolved in 200 mL ethylene glycol and heated to 80°C in a second reaction vessel until a clear solution was obtained (solution B). Subsequently solution A was heated to 80°C and solution B was released into the hot solution within a few seconds. The combined solutions were heated to 160°C. After 2 h the solution was cooled down to room temperature (RT) and the product was separated via centrifugation (4000 rpm for 20 min). The particles were further purified alternately with water and absolute ethanol. Finally, the precipitate was dried at 85°C for 5 h and a white powder was obtained. Taking into account the amount of volatile organic material present in the material (approximately 11 % mass loss according to thermo gravimetric studies) a yield of 75 – 90 % was calculated. The composition of the UCNP is shown in Table 1. The chosen Er^{3+} concentration was small in order to eliminate possible cross relaxation between two excited Er^{3+} ions (see Scheme 1). To calculate the yields of the synthesis for the different as-synthesized UCNP a thermo balance (L81 and STA PT-1600 Fa. Linseis) with simultaneous difference thermal analysis (TG / DTA) was used.

Tab.1: Nomenclature and basic parameters of the $UCNP_{AS}$ investigated. Particle size of $UCNP_{AS}$ nanoparticles were extracted from SEM images as well as calculated based on the Debye-Scherrer equation from XRD pattern.

Parameter	**$UCNP_{AS}$**
Yb^{3+} : Er^{3+}	10:1
Mean diameter (SEM) / nm	41 ± 4
Mean diameter of nanocrystaline domain size (XRD) / nm	31 ± 7
T_{an} / °C	200-700 (for 5h)
Steps of annealing /°C	ΔT = 20 (for 200 -300°C) ΔT = 100 (for 300 -700°C)

2.3. Annealing procedures

The as-synthesized $UCNP_{AS}$ were subjected to annealing at different temperatures T_{an} in a range of 200 °C < T_{an} < 700°C for 5 h using a muffle furnace (LM 212.11, VEB Elektro) to induce a phase transitions in the $NaYF_4$ host lattice (see Table 1). The UCNP materials are denoted as $UCNP_x$ with x = AS for as-synthesized and x = T_{an} (T_{an} = 200°C - 700°C).

2.4. Structural characterization

The size and morphology of as-synthesized UCNP were obtained using a SEM S-4800 scanning electron microscope (Hitachi High-Technologies Canada, Inc., Toronto, Canada) operated with a cold field emission gun (FEG) as cathode and an accelerating voltage of 2kV. The samples were sputtered with platinum in order to reduce the tendency of electrostatic charging.

X-ray powder diffraction (XRD) patterns were collected using a D5005 instrument (Siemens AG, Munich, Germany) in a range of 3-70° / 2θ with divergence aperture, scattering ray aperture and graphite monochromatized Cu K_α radiation (λ = 0.15406 nm). The scanning step was 0.02° / 2θ with a counting time of 4s per step. From the XRD spectra the nanocrystalline domain sizes were calculated using the Debye-Scherer equation (see eq. 1):

$$D = \frac{0.89\,\lambda}{B\cos(\theta)} \qquad (1)$$

D is the domain size to be determined, λ is the wavelength of the x-ray, B is the FWHM of the diffraction peak of interest and θ is the angle of the corresponding diffraction peak.

Raman measurements were carried out using a confocal Raman microscope 300α (WITec Wissenschaftliche Instrumente und Technologie GmbH, Ulm, Germany) equipped with an upright optical microscope. For Raman excitation, laser light at λ = 532 nm was used, which was coupled into a single-mode optical fiber and focused through a 100× objective (Olympus MPlanFL N, NA= 0.9) to a diffraction-limited spot of about 1.3 μm^2. The laser power was set between 0.4 and 1 mW and the integration time was 5 s for all samples under investigation. For the detection the UHTS 300 spectrograph (WITec, Wissenschaft-liche Instrumente und Technologie GmbH, Ulm, Germany) was equipped with a grating (600 lines/mm) and a cooled CCD camera (DU40LA-BR-DD-532, WITec, Wissenschaftliche Instrumente und Technologie GmbH, Ulm, Germany).

2.5. Luminescence characterization

2.5.1. Steady state and time resolved upconversion luminescence

Room temperature steady state and time resolved upconversion emission spectra of the solid samples were obtained using a wavelength tunable pulsed Nd:YAG/OPO laser system (pump laser: Quantaray, Spectra--Physics, Mountain View, CA, USA; OPO: GWU, GWU-Lasertechnik Vertriebsges. mbH, Erftstadt, Germany) operated at 20 Hz as excitation light source and an intensified CCD-camera (iStar DH720-18H-13, Andor Technology, Belfast, Great Britain) coupled to a spectrograph (MS257 Modell 77700A, Oriel Instruments) equipped with a 300 l/mm grating as detector. In order to record the time-resolved luminescence spectra (and subsequently extract the luminescence decay kinetics) the ''box car'' technique was applied. The initial gate delay t_I was set to 500 ns, the gate width was adjusted between 10-100 µs and 350 spectra were measured. For the measurements of the luminescence decay kinetics the time delay between laser excitation pulse and detection window was step-wise increase by the variable gate-step size t_v (see equation 2). This way more data points at shorter times after the laser excitation pulse were acquired in order to ensure a reliable analysis of components with fast luminescence decay kinetics.

$$t(n) = t_I + t_v(n) = t_I + \sum_{i=1}^{n}(i-1)\cdot\ t_k \qquad (2)$$

$t(n)$ consists of t_I, which is a constant of the chosen laser system and the constant step size t_k, which is a luminescence decay dependent system specific parameter. t_v is a variable step size and n (here n = 350) the number of spectra acquired to record the luminescence decay kinetics, which was evaluated by equation 3:

$$I(t) = A + B_1 * exp(-k_1 * t) + B_2 * exp(-k_2 * t) \qquad (3)$$

From the coefficients B_1 and B_2 the relative fractions α_1 and α_2 were calculated according to equation 4:

$$\alpha_1 = \frac{B_1 * \tau_1}{(B_1 * \tau_1 + B_2 * \tau_2)} \qquad (4)$$

The solid samples were measured at room temperature using a specifically designed sample holder for powder samples. The sample holder consists of a cylindrical brass base body with two different thread units. A quartz disc is attached with anodized aluminium cover on one thread. The sample was filled in the base body and sealed with an anodized aluminium stamp. The upconversion luminescence was excited at λ_{ex} = 976 nm.

2.5.2 Time resolved area normalized emission spectra (TRANES)

Measurements for TRANES analysis were carried out using a wavelength tuneable pulsed Nd:YAG/OPO laser system (laser: Quanta Ray, Spectra--Physics, Mountain View, CA, USA; OPO: GWU-Lasertechnik Vertriebsges. mbH, Erftstadt, Germany) operating at 10 Hz as excitation light source (at 26 mJ / 130 mW) and recorded by an intensified CCD-camera (iStar DH 720 18V 73, Andor Technology, Belfast, Great Britain) coupled to a spectrograph (Shamrock SR-303i, Andor Technology, Belfast, Great Britain) equipped with a 600 l/mm grating. The ''box car'' technique was applied for this set of measurements as well (vide supra). The initial gate delay was set to t_I = 500 ns and the gate width was adjusted between δt = 1-30 µs and 300 spectra were measured. For the measurements the time delay between laser excitation pulse and detection window was step-wise increase by a constant gate-step size t_k (see equation 5).

$$t(n) = t_I + t_n(n) = t_I + (n-1)\cdot\ t_k \qquad (5)$$

For the TRANES based component analysis it was considered that a mixed spectra $m(\lambda)$ consists of a combination of the alpha and beta phase spectra $\alpha(\lambda)$ and $\beta(\lambda)$ with the relative fractions C and D, respectively (see equation 6).

$$m(\lambda) = C\ \alpha(\lambda) + D\ \beta(\lambda) \qquad (6)$$

The fractions (C, D) of α- and β-phase were calculated based on the least square method.

3. Results and Discussion

3.1 As-synthesized (cubic) $UCNP_{AS}$

3.1.1 Basic characterization

The as-synthesized sample was first examined by XRD for its phase composition. For the $NaYF_4$ host lattice two different thermodynamically stable phases, the cubic (isotropic) α-phase and the hexagonal (anisotropic) β-phase, are known.[20,48,49]

The XRD diffractogram of $UCNP_{AS}$ with the corresponding *Millerschen indices*[48] of the lattice planes is shown in Figure 1 (left). A comparison of the XRD diffractogram with the database of the International center of diffraction data (ICCD, No. 77-2042) showed that $UCNP_{AS}$ is composed of the cubic α-phase found for $NaYF_4$. The very sharp reflexes of different lattice planes seen in the diffractograms indicate that even though the synthesis was carried out under mild conditions a defined crystal lattice was formed.

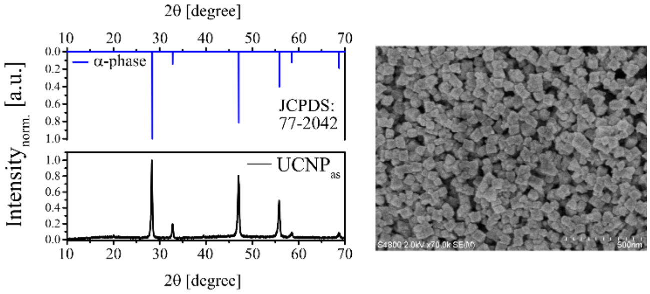

Fig.1: (left) The XRD diffractogram of as-synthesized $UCNP_{AS}$ (and the corresponding reference data from JCPDS) indicate that the sample is composed of the pure cubic α-phase. (right) SEM image (500nm scale) of $UCNP_{AS}$.

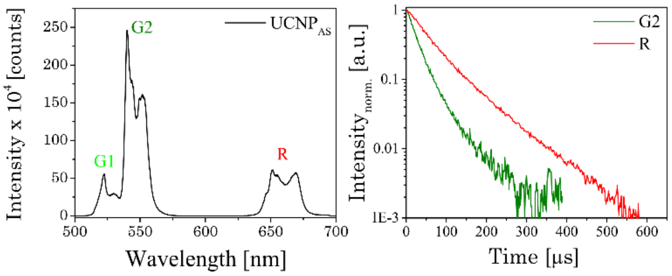

Fig.2: (left) Upconversion luminescence spectrum of the as-synthesized UCNP$_{AS}$. The spectrum was recorded from a powdered sample with λ_{ex} = 976 nm (power density of 191 mW/cm^2). (right) Normalized upconversion luminescence decay kinetics of the Er^{3+} emission bands G2 and R of UCNP$_{AS}$.

The particle size and morphology of UCNP$_{AS}$ was further studied using SEM. The SEM image of UCNP$_{AS}$ show a cubic shape (*Figure 1*, right).[50-53] In order to determine an average particle size from SEM images approximately 500 particles were evaluated. The results of the statistical analysis of the SEM images are shown in Table 1. In addition, the particles size was calculated using the Debye-Scherrer equation. Here, the XRD data were fitted with Lorentz functions and the average particle diameter was obtained. In comparison to the SEM-based size the average diameter is determined approximately 25% smaller. Based on the Debye-Scherrer equation only the crystallite size of the particle is considered in the calculation, which accounts for the observed difference in size found by the two methods. Because of the mild synthesis conditions, the UCNP$_{AS}$ may not be fully crystallized and some amorphous domains may still be present in the particles.

3.1.2. Upconversion luminescence

In Figure 2 (left) the luminescence spectrum of UCNPAS at λ_{ex} = 976 nm is shown. The three typical emission bands can be observed in the green spectral region centered at λ_{em} = 525 nm ($^2H_{11/2} \rightarrow {}^4I_{15/2}$ transition, G1), λ_{em} = 545 nm ($^4S_{3/2} \rightarrow {}^4I_{15/2}$ transition, G2) and in the red spectral region centered at λ_{em} = 660 nm ($^4F_{9/2} \rightarrow {}^4I_{15/2}$ transition, R) (see also Scheme 1).[9,54-57] The observed fine structures (Stark splitting) with in the major emission peaks is induced by the crystal field of the ligands positioned around the Er^{3+} ions in the host lattice.[55,56,58,59]

In Figure 2 (right) the luminescence decay kinetics (λ_{ex} = 976 nm) of UCNP$_{AS}$ are shown measured at the emission bands G2 and R, respectively. For the emission bands G2 and R a distinctly different time dependence of the luminescence was observed (see *Figure 2*, right), whereas no difference between G1 and G2 was observed (see *SI.Fig. 1*). In the data analysis a bi-exponential decay law was applied.[55,60,61] As a trend, the calculated luminescence decay times (τ_1 and τ_2) were longer for the red emission band (R) compared to the green emission bands (G1, G2).

Tab.2: Luminescence decay times τ with the different time components and relative fractions of the as-synthesized UCNP$_{AS}$ for the emission bands G2 and R, respectively.

Decay time	UCNP$_{AS}$	Relative Fraction [%]
$\tau_{G2,1}$ [µs]	23±1	71
$\tau_{G2,2}$ [µs]	65±5	29
$\tau_{R,1}$ [µs]	51±1	64
$\tau_{R,2}$ [µs]	118±6	36

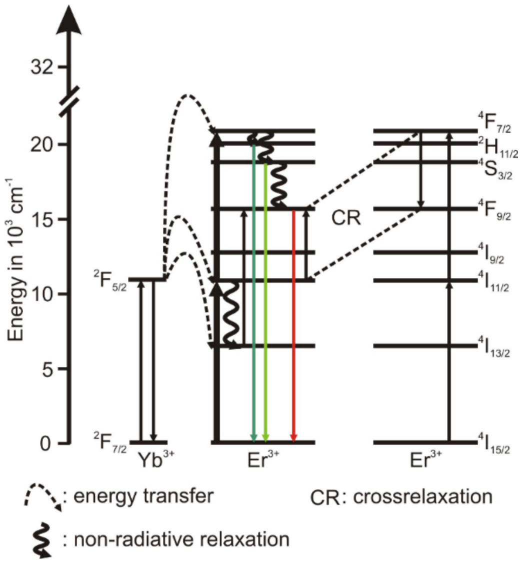

Scheme 1: Schematic energy level diagram for the upconversion related processes of the Yb^{3+} (sensitizer) Er^{3+} (activator) system following an excitation at λ_{ex} = 976 nm. The full lines pointing upwards represent absorption, the dotted lines represent energy transfer, the waved lines represents non-radiative relaxation processes and the colored full lines pointing downwards represents emission. The cross-relaxation between two excited Er^{3+} ions is represented by "CR".

3.2 Annealed UCNP$_x$

The $NaYF_4$ lattice shows a phase transition from cubic to hexagonal and as a consequence the upconversion properties of UCNP are distinctly influenced due to structure-related parameters like lattice vibrations. To study the phase transfer from the cubic (α) to the hexagonal (β) phase in more detail the UCNP$_{AS}$ were annealed at different temperatures T$_{an}$.

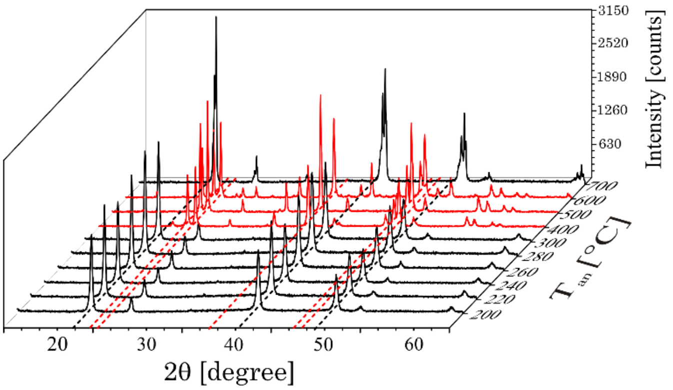

Fig.3: Suited selection of X-ray diffraction patterns of UCNP$_x$ after annealing between 200°C < T$_{an}$ < 700°C for 5h. The black dotted lines correspond to the position of reflexes of the cubic phase whereas red dotted lines correspond to the position of reflexes of the hexagonal phase, respectively.

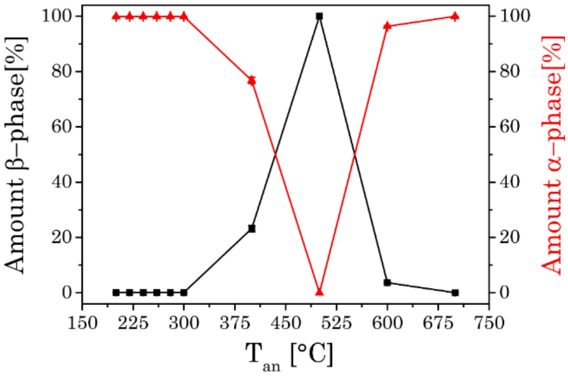

Fig.4: Amount of α- and β-phase in correlation to temperature of the thermal treatment, calculated on the intensity of the different XRD reflexes of α- and β-phase.

At T_{an} > 400°C the nanoparticles tend to build up micro-domains (see *SI.Fig. 2*), therefore the samples are further denoted as $UCNP_x$ materials.[7]

3.2.1 XRD

In Figure 3 selected XRD diffraction patterns of $UCNP_x$ after annealing in the temperature range of 200°C < T_{an} < 700°C for 5h are shown. The overall intensity of the diffraction patterns was increased with increasing temperature T_{an} (see *SI.Fig.3*), whereas the FWHM of the different peaks stayed unaltered (see *SI.Fig.3*). The increase in intensity is a good indication for an improved crystallinity of the $UCNP_x$ upon annealing. The crystallite size was calculated using the *Debye Scherrer* equation (see *SI.Table 1*). It is obvious that there is a slightly increase of the crystallite size for UCNP annealed at T_{an} < 300°C, whereas for 300°C < T_{an} < 600°C an significant increase of the crystallite size was found due to the change of the crystal phase of the host lattice and the formation of micro domains. In Figure 3 for annealing temperatures below 300°C only the cubic phase is observed in the XRD spectra, while for a annealing temperature of T_{an} = 400°C the hexagonal phase is clearly seen as the major crystal phase. The relative fraction of this phase gradually increased with increasing T_{an} up to 500°C. Based on the XRD data (for 400°C < T_{an} < 500 °C only a minor amount of cubic phase seems to be present in the material (see *Figure 4*). A further increase of T_{an} > 500 °C lead however to a decrease of the hexagonal phase and at T_{an} = 700°C again mainly the cubic phase was found in the XRD diffractograms. From Figure 3 it can be seen that the $UCNP_{700}$ material is slightly different in the observed XRD peak pattern indicating that the phase back transfer may not be fully completed. This has been observed before for bulk material by *Hebert et. al*.[62-64]

3.2.2 Raman spectroscopy

In the Raman spectra of $UCNP_{AS}$ (cubic phase) two dominant broad bands around ν = 275 cm^{-1} and 745 cm^{-1} were observed, which were also found for $UCNP_x$ annealed up to T_{an} < 300°C. Moreover, the comparison of the samples annealed at T_{an} < 300°C and the sample annealed at T_{an} = 700°C showed only small differences with respect to peak position and spectral distribution (see *Figure 5, left top*). These results are complementary to the corresponding XRD data (vide supra) pointing to a cubic phase for the respective materials. The Raman spectra of the hexagonal phase materials display five main peaks at ν = 251 cm^{-1}, 303 cm^{-1}, 359 cm^{-1}, 492 cm^{-1} and 625 cm^{-1}, whereas the high phonon vibrational bands ν > 700 cm^{-1}, which have been found for the cubic phase materials, are only weakly present (see *Figure 5*). The observed alterations in the Raman spectra are well correlated with the phase transition of the host lattice seen in the XRD diffractograms. Moreover, also the small differences between the sample annealed at T_{an} = 700°C and samples for T_{an} < 300°C is confirmed by the Raman spectra (see *Figure 5*).

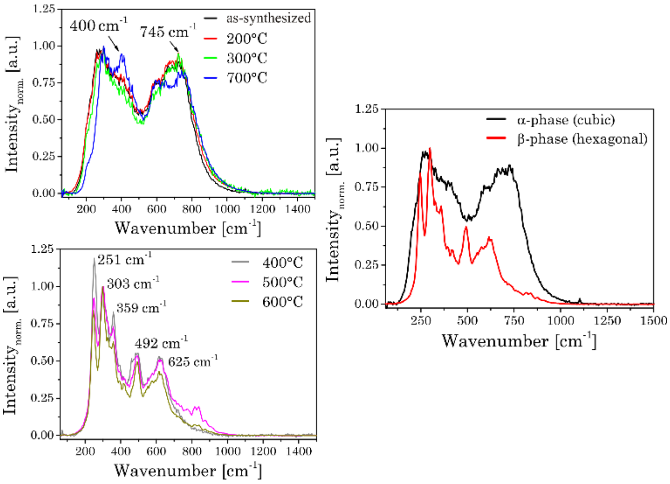

Fig.5: (left) Normalized Raman spectra of as-synthesized $UCNP_{AS}$ and annealed $UCNP_x$. (right) Representative Raman spectra of α- and β-phase.

3.2.3 Upconversion Luminescence

The upconversion luminescence of the UCNP materials investigated in detail using (quasi) steady state and time-resolved luminescence techniques. In the (quasi) steady state luminescence measurements a detection window of 500 µs

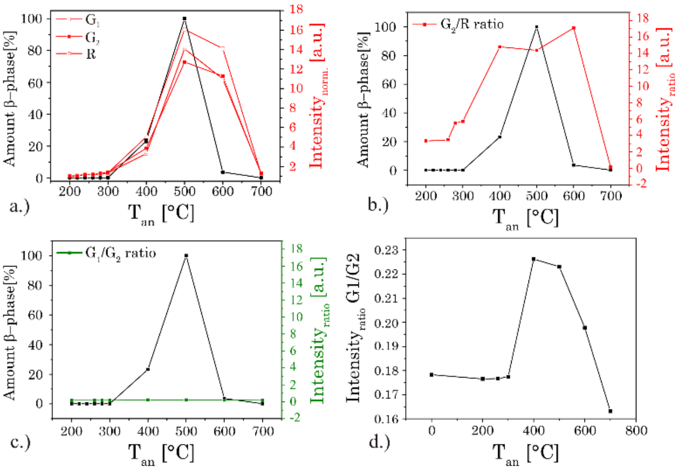

Fig.6: (a.) Alteration in the (quasi) steady state intensity of the different luminescence bands with annealing temperature T_{an}. The ratio G2/R (b.) and G1/G2 (c.) based on the integrated steady state luminescence intensity of these emission bands and amount of hexagonal β-phase, both as function of temperature T_{an}. The amount of β-phase was calculated based on XRD measurements. (d.) Enlargement of the G1/G2 ratio over T_{an}.

was used collecting more than 95% of the overall luminescence intensity. In the upconversion luminescence spectra the intensity as well as the spectral intensity distribution was altered due to the annealing (see *Figure 6*). For T_{an} < 300°C a small increase in the upconversion luminescence intensity was found, but no alteration in the spectral intensity distribution was observed (see SI-Fig.4). For annealing temperatures in the range of 300°C < T_{an} < 600°C a distinct increase in the overall upconversion luminescence intensity was found with a maximum at T_{an} = 500 °C.[18,68-70] In addition, for this set of samples the spectral intensity distribution was changed as well. Within the different emission bands (G1, G2, and R) Stark level-related substructures became apparent, but also the relative contribution of the G- and R-bands was altered (see *Figure 6*).

While the ratio of G1/G2 was found to be nearly independent on the annealing temperature the ratio G2/R showed a distinct change for T_{an} > 300°C (see *Figure 6*). The sample obtained at T_{an} = 700°C showed a reversed effect, here the overall intensity as well as the spectral intensity distribution were changed back according to materials obtained for T_{an} < 300°C. In Figure 6 the overall intensity, the ratio G2/R (as well as the G1/G2 ratio), and the amount of β phase in the different samples are compared. The spectral changes are well correlated with the phase transition from the cubic (α) phase to the hexagonal (β) phase corroborating the results of the XRD and Raman measurements.[34,41,44] In addition, for high T_{an} a reduction in lattice defects due to the annealing process and a subsequent decrease of radiationless deactivation improving the energy migration between Yb^{3+} ions within the crystal may also have a positive effect on the overall upconversion luminescence intensity.

3.2.4 Laser power dependent luminescence measurements

The UC luminescence intensity (I_{UC}) is proportional to the "*n*"th of excitation power (I_{IR}) (see *equation 7*).

$$I_{UC} \sim I_{IR}^{n} \quad (7)$$

n is the number of absorbed NIR photons per visible photon emitted and can be obtained from the slope of log (I_{UC}) versus log (I_{IR}) analysis (see *Figure 7*).[61,72-76]

For the G1 and G2 luminescence two NIR photons need to be transfered (*n* = 2, see *Figure 7*) from two Yb^{3+} ions (sensitizer) to one Er^{3+} ion (activator).[61,72,73]

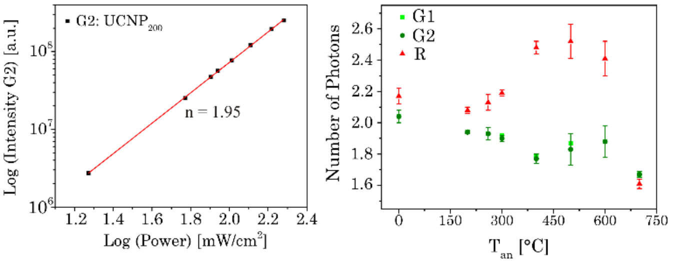

Fig. 7: (left) Dependence of upconversion luminescence intensity on laser power for G2 related emission of $UCNP_{200}$. (right) n-values determined for the emission bands G1, G2, and R for $UCNP_x$ annealed at different T_{an}.

First, the $^4I_{11/2}$ energy level and then the $^4F_{7/2}$ energy level of Er^{3+} is populated. Followed by a non radiative deactivation from the $^4F_{7/2}$ to the $^2H_{11/2}$ energy level (G1) or further to the $^4S_{3/2}$ energy level (G2). Alternatively the $^4S_{3/2}$ energy level can also be deactivated non radiatively through multiphonon interaction with the host lattice to the $^4F_{9/2}$ energy level yielding the emission band R (also via two energy transfer steps, *n* = 2). In addition, the $^4F_{9/2}$ energy level can be populated via two different three photon energy transfer process (*n = 3*).[20,55,56,67,77] The $^4S_{3/2}$ energy level of one Er^{3+} ion is populated by two energy transfer steps from excited Yb^{3+} ions whereas a second Er^{3+} ion is in the $^4I_{11/2}$ energy level via one energy transfer step from Yb^{3+}. Following a cross relaxation between the two excited Er^{3+} ions both Er^{3+} ions reached the $^4F_{9/2}$ energy level from which the red emission (R) can occur (three photon process A). The three photon process A is only possible at high Er^{3+} concentration and can be neglected in our materials due to the low Er^{3+} concentration.[57,67,78-80] In a second three photon process B the $^4S_{3/2}$ energy level of the Er^{3+} ion is populated by two energy transfer steps from excited Yb^{3+} ions. Then, the $^4I_{13/2}$ level of Er^{3+} can be populated via an energy back transfer (BET) from the $^4S_{3/2}$ level of Er^{3+} to neighbouring Yb^{3+} ions [81]. A subsequent energy transfer from excited Yb^{3+} ions to the $^4I_{13/2}$ level of Er^{3+} leads to the population of the $^4F_{9/2}$ energy level and the red emission band R.[82] The n-value for G1 and G2 is slightly, but steadily decreased with increasing annealing temperature from *n* ~ 2 ($UCNP_{AS}$) to *n* ~ 1.7 (for T_{an} = 700°C) (see *Figure 7, right*). In contrast the *n*-value for the R band increased from *n* ~ 2.1 ($UCNP_{AS}$) to *n* ~ 2.5 (T_{an} = 600°C). A distinct difference in the n-values is found for cubic phase ($UCNP_{AS}$) and hexagonal phase ($UCNP_{400}$), but already at T_{an} < 400 °C a slight but steady change in the *n*-values was observed (see *Figure 7 (right)*). Opposing effects originating from the differences in phonon coupling in cubic and hexagonal lattice as well as from the interplay between radiationless deactivation and saturation effects at higher laser power may be the reason for the observed trends in *n* for the G and R band(s), respectively. While for the green emission bands G1 and G2 theoretically *n* = 2 is expected and the observed decrease of *n* with increasing T_{an} points toward a saturation effect, for the R band the change in the matrix-related phonon coupling is the major factor responsible for the overall increase of *n*.[61,83] To further elucidate the different factors the power dependence of the spectral intensity distribution was analyzed in more detail. In Figure 8 the ratio of the green luminescence bands G1/G2 (left) as well as the ratio

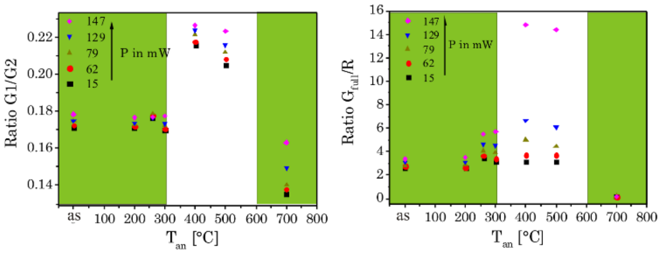

Fig.8: Peak ratio G1/G2 (left) and G_{full}/R (right) versus annealing temperature at different laser power P. The green inlet represents the alpha phase and the white inlet the beta phase of the host lattice (λex = 976 nm).

of the overall green and red luminescence G_{full}/ R (right) is shown for different laser power (λ_{ex} = 976 nm). For the G1/G2 ratio almost no influence of the laser power is found for the $UCNP_x$ annealed at T_{an} < 300°C. For T_{an} > 300°C a slight jump in the G1/G2 ratio was found but no significant influence of the laser power. The observed "jump" falls well within the range of T_{an} for which the hexagonal phase is dominant.[72,74] At T_{an} = 700°C a decrease and a slight power dependence was observed for the G1/G2 ratio. It is known that the G1 is mainly populated via thermal excitation from the $^4S_{3/2}$ level (G2). The energy gap between the $^4S_{3/2}$ – and $^2H_{11/2}$ level is decreased due to the thermal treatment (associated therewith phase transfer from α- to β-phase) and leads to a more efficient thermal population of the $^2H_{11/2}$ level, subsequently increasing the G1/G2 ratio (see *Figure 8*, left). In contrast, for the G_{full}/R ratio a distinct laser power dependence was found. Especially in the range of 300°C < $T_{an} \leq$ 600°C representative for the hexagonal phase a large increase by a factor of about 7 was measured (see *Figure 8*, right). As for the G1/G2 ratio at T_{an} = 700°C the G_{full}/R ratio dropped back (even below) to the value found for T_{an} < 300°C and the laser power influence disappeared. The energy mismatch of the $^2F_{5/2}$ level of Yb^{3+} and the $^4I_{11/2}$ level of Er^{3+} is smaller in the hexagonal phase than in the cubic phase and a better phonon matched energy transfer process between Yb^{3+}- and Er^{3+}- ions is possible which accounts for the observed lattice phase influence (especially for the G1/G2 ratio). The possibility of saturation effects (e.g., BET, cross relaxation) might be increased as well due to the improved phonon matching. In case of the G_{full}/R ratio the alteration of the R is the dominant factor. In case of a high concentration of excited Yb^{3+} ions (sensitizers) the activation into the $^4F_{7/2}$ state becomes faster and can successfully compete with the radiationless deactivation from the $^4I_{11/2}$ into the $^4I_{13/2}$ state, which is a necessary prior step before the activation into the $^4F_{9/2}$. From $^4F_{9/2}$ state subsequently R emission occurs (see Scheme 2).

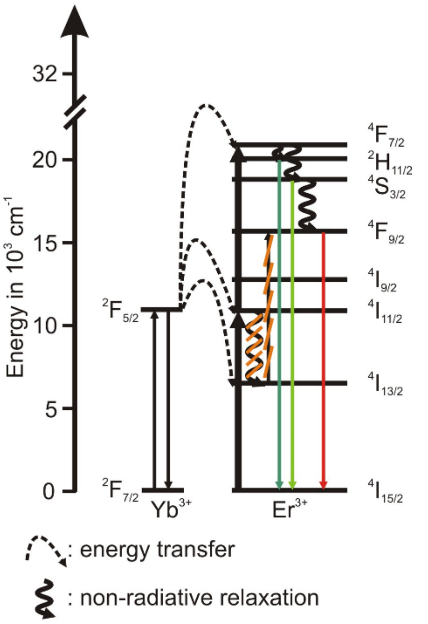

Scheme 2: Energy scheme of the upconversion processes in the hexagonal phase with suppressed population route of the $^4F_{9/2}$ level (underlined by the orange lines).

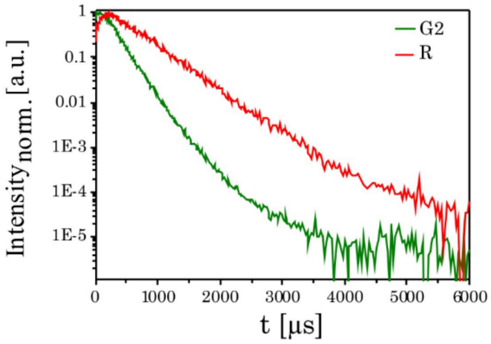

Fig.9: Normalized upconversion luminescence decays of the G2 and R bands of Er^{3+} in $UCNP_{300}$ (λ_{ex} = 976 nm).

3.2.5 Time-resolved luminescence

The luminescence decay kinetics of the $UCNP_X$ materials showed a complex time dependence. In Figure 9 the luminescence decay kinetics (λ_{ex} = 976 nm) of $UCNP_{300}$ are shown for the two emission bands G2 and R. It can be seen that the kinetics of the two bands show a distinctly different time dependence.

For R an initial rise in the luminescence intensity is observed (for t < 500 µs, see *Figure 9*). The complexity of the observed decay kinetics could be a result of the contributions from Er^{3+} ions located in different chemical environments (e.g., surface vs. volume effects, amorphous domains, which are reduced due to annealing). The experimental data of G1, G2 and R were analyzed by a bi-exponential decay kinetics.

Luminescence decay times τ_1 and τ_2 were calculated for the different bands G1, G2 and R of the $UCNP_X$ materials. An increase in both luminescence decay times with increasing T_{an} was found. Moreover, at T_{an} > 300°C for both luminescence decay times an accelerated increase with increasing T_{an} was calculated (see *Figure 10*). This trend in the decay time is accompanied by the crystal phase transfer from cubic to hexagonal (vide supra). The drop observed for τ_1 and τ_2 at T_{an} = 700°C (here, the material switched back to a cubic phase) supports the correlation of the luminescence decay kinetics and the lattice phase. The results of the luminescence kinetics measurements are in very good agreement with the other spectroscopic data presented for the G1/G2 and G_{full}/R ratio.

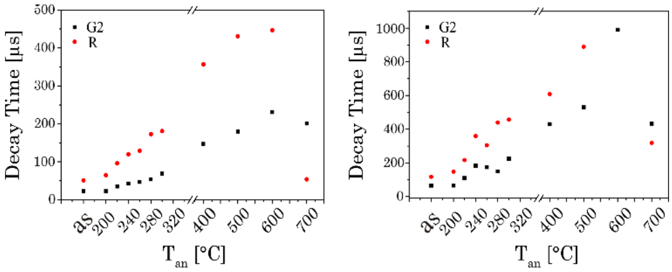

Fig.10 : Luminescence decay times of UCNPs annealed at different T_{an} for the emission bands G2 and R, (left) the short decay component, (right) the long decay component (λ_{ex} = 976 nm).

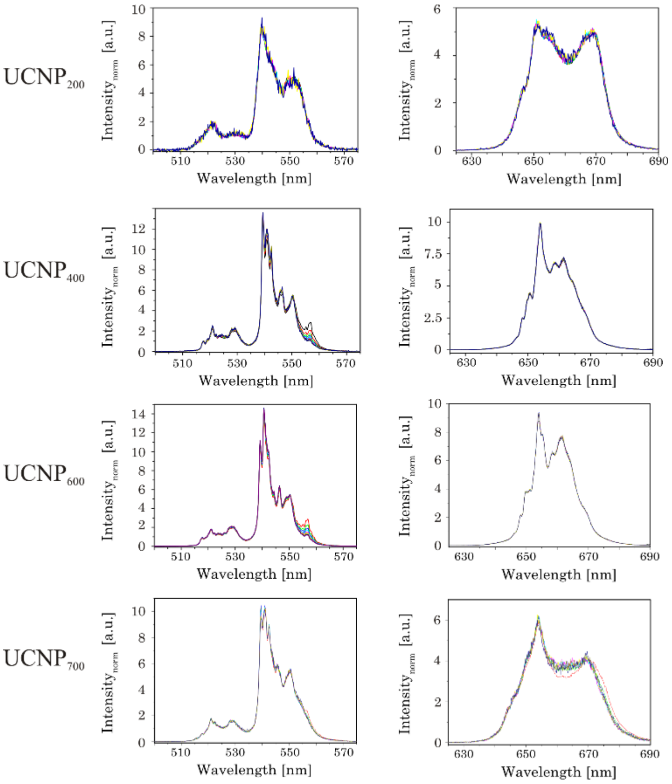

Fig.11: TRANES of annealed UCNP$_x$ (200°C < x < 700°C) for (left) G1 and G2 luminescence as well as (right) of R luminescence are shown (λ_{ex} = 976 nm). The delay after the laser pulse was varied between 0 µs and 2000 µs.

3.2.6 Time-resolved area normalized emission spectra (TRANES)

In order to pinpoint the influence of the lattice on the luminescence upconversion the time-resolved emission spectra were evaluated by TRANES analysis. TRANES can be used to reveal small time-dependent variations in the spectral intensity distribution of a luminescence spectrum. They were calculated from the time-resolved emission spectra recorded for the determination of the luminescence decay kinetics by normalizing the area of the emission spectrum recorded at different delay times after the laser pulse (e.g., area of spectrum is normalized to one). In Figure 11 (top) the TRANES of UCNP$_{200}$ are shown. No change in the spectral intensity distribution neither for the G1 and G2 luminescence nor for the R luminescence is detected. For UCNP$_{300}$ a significant change in the intensity distribution of the luminescence is found for G1 and G2 as well as for R (see *Figure 12*). In the TRANES isoemissive points are found. E.g., for G1 isoemissive points can be seen at λ_{em} = 516.8 nm, 521.8 nm and 523.2 nm and the luminescence peak at λ_{em} = 529 nm becomes more pronounced (see *Figure SI-4*). Also in the case of G2 the intensity distribution is altered with increasing delay relative to the excitation pulse. For the R luminescence two isoemissive points are identified at λ_{em} = 651 nm and 665.8 nm. Furthermore, the shoulder at λem = 668 nm is decreased whereas a completely new peak appears at λem = 661 nm. In Figure 11 the upconversion emission spectra for UCNP400 and UCNP600 are shown as well. The variations in the spectral intensity distribution of G1 and G2 as of R are small for both materials (the luminescence intensity distribution is only slightly changed for the emission band G2). For the TRANES analysis of UCNP$_{700}$ it can be seen that the spectral intensity distribution remains unchanged with increasing delay time. Moreover, a comparison with the spectra of UCNP$_{200}$ – UCNP$_{600}$ materials shows that for the UCNP$_{700}$ material a close resemblance to the UCNP$_{200}$ material is found (especially for the R luminescence). The results of the TRANES analysis nicely complement the data of the other experimental techniques reflecting the phase transition from cubic to hexagonal (and back to cubic) upon annealing in the temperature range 200°C < T_{an} < 700°C. However, while the other analytical techniques and data evaluation approaches gave only a rough picture of the phase transfer and its start temperature T_{an}, in the TRANES analysis of the G1, G2 and R emission bands already small fractions of hexagonal phase could be detected. The fact, that the shape of the emission bands is changed with increasing delay time after the laser pulse in favor of the hexagonal phase related luminescence, is a consequence of the significant differences in the decay times of Er^{3+} luminescence in the two lattice phases involved due to difference in the symmetry of the chemical environment (*vide supra*). Consequently the relative luminescence intensity contribution of Er^{3+} ions located in the cubic and hexagonal

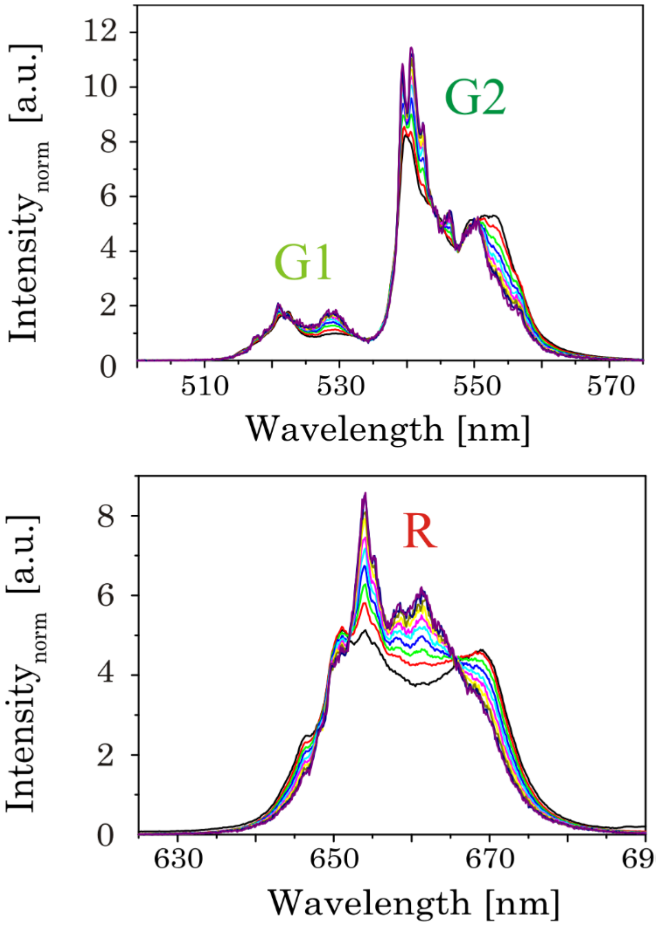

Fig. 12: TRANES of annealed UCNP$_{300}$ for (up) G1 and G2 luminescence as well as (below) of R luminescence are shown (λex = 976 nm). The delay after the laser pulse was varied between 0 µs and 2000 µs (displayed by the colors in 120 µs steps).

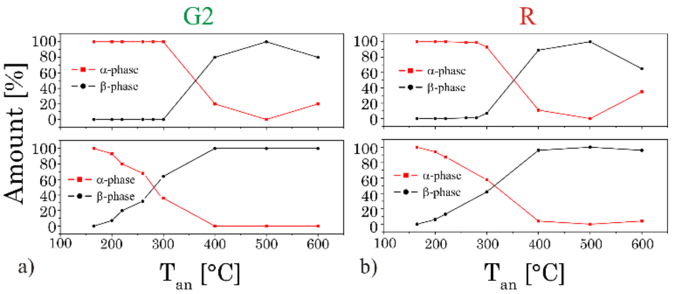

Fig. 13: Variation of the amount of different crystal phase (α- and β-phase) calculated out of the TRANES analysis at delay times after the laser pulse (top: 0 µs and bottom: 500 µs) for emission band G2 (a) and R (b).

phase changes with time after the laser pulse and the different lattice environments, if present, can be identified in the sample from the alteration in the spectral intensity distribution. The TRANES analysis is very sensitive and allows to analyze even small difference in the material composition. The small differences in the intensity distribution of G1 and G2 of the $UCNP_{700}$ material compared to $UCNP_{200}$ indicate a small fraction of hexagonal phase to be still present in this material. For a complete back transfer to the cubic phase higher temperatures or/and longer annealing times seem to be necessary. Based on the diffractogram and the corresponding Debye-Scherrer calculations an increase in the crystallite size as well as an asymmetric growth of the UCNP was found, which could also have an impact on the intensity distribution of G1 and G2 of the $UCNP_{700}$ material. Based on the approximation that in the $UCNP_{AS}$ and the $UCNP_{500}$ only cubic and hexagonal phase, respectively, are present, a spectral decomposition of the emission spectra recorded at a delay time of 0 µs and 500 µs was performed in order to calculate the relative amount of cubic and hexagonal phase for the different $UCNP_x$ materials (see *Figure 13*). It can be seen, that in the temperature range of 200°C < T_{an} < 400°C a gradual transformation of the cubic into the hexagonal phase is already present.

4. Conclusion

$NaYF_4$ nanoparticles co-doped with Er^{3+} and Yb^{3+} were synthesized under mild conditions using PVP 40 as capping agent and as stabilizer, respectively. The $UCNP_{AS}$ were uniform in size and shape with a cubic crystal lattice. After the annealing between 200°C < T_{an} < 700°C for 5h changes in crystal lattice phase and subsequently in the upconversion luminescence properties of the UCNP materials were induced. The lattice phase and structure of the UCNP materials obtained at different T_{an} were analyzed using XRD, Raman spectroscopy as well as SEM. The upconversion luminescence properties of the annealed UCNP materials were studied by steady state and time resolved luminescence. Upconversion luminescence proved to be a sensitive tool to monitor the phase transition of the host lattice. While based on XRD and Raman spectroscopy no clear indication for a change in the lattice phase was found for T_{an} < 300°C, the upconversion luminescence proved to be more sensitive capable of resolving even small contributions of cubic and hexagonal phase, respectively, in the materials. Based on the upconversion fluorescence studies of the $UCNP_X$ materials the complex interplay of the host lattice crystal phases and the population routes of the Er^{3+} energy levels involved in the upconversion processes was evaluated. The laser power dependence of the green (G1, G2) and red (R) luminescence was found to be dependent on the annealing temperature. In addition, green and red luminescence was found to respond differently on the host lattice phase. A major population route of the R luminescence is attenuated at higher laser power, which is more efficient for the hexagonal lattice phase, the relative contributions expressed as the ratio between G_{full} and R is altered (see Scheme 2). Although already regular upconversion data, like spectral intensity distribution from steady state luminescence measurements or luminescence decay kinetics, show a clear lattice phase dependent behavior, TRANES analysis proved to be superior. The basis for the full exploitation of the power of TRANES is the different luminescence decay kinetics of the upconversion in cubic and hexagonal lattice phase. While the analysis of the luminescence kinetics with respect to physical meaning full luminescence decay times is difficult due to the complex time dependence and the related challenges in the data analysis, TRANES employs a combination of time and spectral information. Based on TRANES even minor amounts of cubic or hexagonal phase could be identified in the different UCNP materials. TRANES could also be a great tool for monitoring the phase composition of UCNP *in situ* during synthesis.[84,85]

Acknowledgements

We are thankful to Dr. C. Günter and Dr. C. Prietzel (work group of Prof. J. Kötz) for XRD and SEM measurements of the samples, respectively.

References

1 Z. Li and Y. Zhang, Angew. Chemie - Int. Ed., 2006, 45, 7732–7735.

2 J. Yin, Y. Hu and J. Yoon, Chem. Soc. Rev., 2015, 44, 4619–4644.

3 N. Kaur, W. Hyland and J. F. Callan, Chem. Soc. Rev., 2015, 44, 4415–4432.

4 T. D. Ashton, K. a. Jolliffe and F. M. Pfeffer, Chem. Soc. Rev., 2015, 44, 4547–4595.

5 Y. Tang, D. Lee, J. Wang, G. Li, J. Yu, W. Lin and J. Yoon, Chem. Soc. Rev., 2015, 44, 5003–5015.

6 L. Niu, Y. Chen, H. Zheng, L. Wu, C. Tung and Y. Chen, Chem. Soc. Rev., 2015, 44, 6143–6160.

7 G. Yi, H. Lu, S. Zhao, Y. Ge and W. Yang, Nano Lett., 2004, 4, 2191–2196.

8 J. Shan, W. Kong, R. Wei, N. Yao and Y. Ju, J. Appl. Phys., 2010, 107, 054901.

9 K. Wu, J. Cui, X. Kong and Y. Wang, J. Appl. Phys., 2011, 110, 053510–053515.

10 J. Shen, Y. Zhu, X. Yang and C. Li, Chem. Commun., 2012, 48, 3686.

11 S. Zhu, J. Zhang, C. Qiao, S. Tang, Y. Li, W. Yuan, B. Li, L. Tian, F. Liu, R. Hu, H. Gao, H. Wei, H. Zhang, H. Sun and B. Yang, Chem. Commun. (Camb)., 2011, 47, 6858–6860.

12 M. Montalti, A. Cantelli and G. Battistelli, Chem. Soc. Rev., 2015, 44, 4853–4921.
13 S. Silvi and A. Credi, Chem. Soc. Rev., 2015, 44, 4275–4289.
14 K. D. Wegner, N. Hildebrandt and N. Hildebrandt, Chem. Soc. Rev., 2015, 44, 4792–4834.
15 O. S. Wolfbeis, Chem. Soc. Rev., 2015, 44, 4743–4768.
16 H. Peng and D. T. Chiu, Chem. Soc. Rev., 2015, 44, 4699–4722.
17 J. Thomas, Chem. Soc. Rev., 2015, 44, 4494–4500.
18 J. Zhou, Z. Liu and F. Li, Chem. Soc. Rev., 2012, 41, 1323.
19 Q. Liu, Y. Sun, T. Yang, W. Feng, C. Li and F. Li, J. Am. Chem. Soc., 2011, 133, 17122–17125.
20 F. Wang, Y. Han, C. S. Lim, Y. Lu, J. Wang, J. Xu, H. Chen, C. Zhang, M. Hong and X. Liu, Nature, 2010, 463, 1061–1065.
21 E. M. Chan, Chem. Soc. Rev., 2015, 44, 1653–1679.
22 N. M. Idris, M. K. G. Jayakumar, A. Bansal and Y. Zhang, Chem. Soc. Rev., 2014, 44, 1449–1478.
23 A. Sedlmeier and H. H. Gorris, Chem. Soc. Rev., 2014, 44, 1526–1560.
24 M.-K. Tsang, G. Bai and J. Hao, Chem. Soc. Rev., 2015, 44, 1585–1607.
25 D. Yang, P. Ma, Z. Hou, Z. Cheng, C. Li and J. Lin, Chem. Soc. Rev., 2014, 44, 1416–1448.
26 W. Zheng, P. Huang, D. Tu, E. Ma, H. Zhu and X. Chen, Chem. Soc. Rev., 2014, 44.
27 L. Prodi, E. Rampazzo, F. Rastrelli, A. Speghini and N. Zaccheroni, Chem. Soc. Rev., 2015, 44, 4922–4952.
28 H. Guo, Z. Li, H. Qian, Y. Hu and I. N. Muhammad, Nanotechnology, 2010, 21, 125602.
29 J. Jin, Y.-J. Gu, C. W.-Y. Man, J. Cheng, Z. Xu, Y. Zhang, H. Wang, V. H.-Y. Lee, S. H. Cheng and W.-T. Wong, ACS Nano, 2011, 5, 7838–47.
30 G. Chen, T. Y. Ohulchanskyy, R. Kumar, H. Ågren and P. N. Prasad, ACS Nano, 2010, 4, 3163–3168.
31 Q. Cheng, J. Sui and W. Cai, Nanoscale, 2012, 4, 779.
32 F. Auzel, Chem. Rev., 2004, 104, 139–173.
33 F. Auzel, J. Lumin., 1990, 45, 341–345.
34 H. H. Gorris and O. S. Wolfbeis, Angew. Chemie, 2013, 125, 3668–3686.
35 F. Wang and X. Liu, Chem. Soc. Rev., 2009, 38, 976–989.
36 X. Chen, D. Peng, Q. Ju and F. Wang, Chem. Soc. Rev., 2014, 44, 1318–1330.
37 L. Tu, X. Liu, F. Wu and H. Zhang, Chem. Soc. Rev., 2015, 44, 1331–1345.
38 G. Liu, Chem. Soc. Rev., 2014, 44, 1635–1652.
39 M. He, P. Huang, C. Zhang, H. Hu, C. Bao, G. Gao, R. He and D. Cui, Adv. Funct. Mater., 2011, 21, 4470–4477.
40 K. Gavvala, R. K. Koninti, A. Sengupta and P. Hazra, *Phys. Chem. Chem. Phys.*, 2014, **16**, 14953.
41 S. N. Lee, J. Park, M. Lim and T. Joo, *Phys. Chem. Chem. Phys.*, 2014, **16**, 9394.
42 A. Chatterjee and D. Seth, *Photochem. Photobiol. Sci.*, 2013, 369–383.
43 T. Shanmugapriya, R. Vinayakan, K. G. Thomas and P. Ramamurthy, *CrystEngComm*, 2011, **13**, 2340.
44 B. Carlotti, E. Benassi, A. Cesaretti, C. G. Fortuna, A. Spalletti, V. Barone and F. Elisei, *Phys. Chem. Chem. Phys.*, 2015, **17**, 20981–20989.
45 B. Carlotti, a. Cesaretti, C. G. Fortuna, a. Spalletti and F. Elisei, *Phys. Chem. Chem. Phys.*, 2015, **17**, 1877–1882.
46 F. Meng, S. Liu, Y. Wang, C. Tao, P. Xu, W. Guo, L. Shen, X. Zhang and S. Ruan, J. Mater. Chem., 2012, 22, 22382.
47 L. Wang, R. Yan, Z. Huo, L. Wang, J. Zeng, J. Bao, X. Wang, Q. Peng and Y. Li, Angew. Chemie - Int. Ed., 2005, 44, 6054–6057.
48 L. Wang, X. Xue, H. Chen, D. Zhao and W. Qin, Chem. Phys. Lett., 2010, 485, 183–186.
49 H. Li and L. Y. Wang, Chinese Sci. Bull., 2013, 58, 4051–4056.
50 B. Voß, J. Nordmann, A. Uhl, R. Komban and M. Haase, Nanoscale, 2013, 5, 806–12.
51 R. Komban, J. P. Klare, B. Voss, J. J. Nordmann, H.-J. H.-J. Steinhoff and M. Haase, Angew. Chemie-International Ed., 2012, 51, 6506–6510.
52 Q. Tian, K. Tao, W. Li and K. Sun, 2011, 22886–22892.
53 J. Shan and Y. Ju, Nanotechnology, 2009, 20, 275603.
54 J. Shan, M. Uddi, N. Yao and Y. Ju, Adv. Funct. Mater., 2010, 20, 3530–3537.
55 J. F. Suyver, J. Grimm, K. W. Krämer and H. U. Güdel, J. Lumin., 2005, 114, 53–59.
56 and H. U. G. A. Shalav, B.S. Richards, K.W. Krämer, Conf. Rec. IEEE Photovolt. Spec. Conf., 2005, 31, 114–117.
57 F. Vetrone, J. C. Boyer, J. A. Capobianco, A. Speghini and M. Bettinelli, J. Phys. Chem. B, 2003, 107, 1107–1112.
58 S. V Eliseeva and J.-C. G. Bünzli, Chem. Soc. Rev., 2010, 39, 189–227.
59 J. M. F. van Dijk, J. Chem. Phys., 1983, 78, 5317.
60 J. Zhao, Z. Lu, Y. Yin, C. McRae, J. a Piper, J. M. Dawes, D. Jin and E. M. Goldys, Nanoscale, 2013, 5, 944–52.
61 W. Yu, W. Xu, H. Song and S. Zhang, Dalt. Trans., 2014, 43, 6139–6147.
62 R. Thoma, H. Insley and G. Hebert, Inorg. Chem., 1966, 1005, 1222–1229.
63 R. E. Thoma, C. F. Weaver, H. a. Friedman, H. Insley, L. a. Harris and H. a. Yakel, J. Phys. Chem., 1961, 65, 1096–1099.
64 K. W. Krämer, D. Biner, G. Frei, H. U. Güdel, M. P. Hehlen and S. R. Lüthi, Chem. Mater., 2004, 16, 1244–1251.
65 Y. Song, Q. Tian, R. Zou, Z. Chen, J. Yang and J. Hu, J. Alloys Compd., 2011, 509, 6539–6544.
66 S. Wilhelm, T. Hirsch, W. M. Patterson, E. Scheucher, T. Mayr and O. S. Wolfbeis, Theranostics, 2013, 3, 239–248.
67 J. F. F. Suyver, J. Grimm, M. K. K. van Veen, D. Biner, K. W. W. Krämer and H. U. U. Güdel, J. Lumin., 2006, 117, 1–12.
68 S. Schietinger, L. D. S. Menezes and O. Benson, Nano Lett., 2009, 9, 2477–2481.
69 S. Mishra, G. Ledoux, E. Jeanneau, S. Daniele and M.-F. Joubert, Dalt. Trans., 2012, 41, 1490.
70 M. Wang, G. Abbineni, A. Clevenger, C. Mao and S. Xu, Nanomedicine Nanotechnology, Biol. Med., 2011, 7, 710–729.
71 Y. Chen, W. He, H. Wang, X. Hao, Y. Jiao, J. Lu and S. Yang, J. Lumin., 2012, 132, 2404–2408.
72 J. Shan, M. Uddi, R. Wei, N. Yao and Y. Ju, 2009, 2452–2461.
73 D. Lu, S. K. Cho, S. Ahn, L. Brun, C. J. Summers and W. Park, ACS Nano, 2014, 7780–7792.
74 J. F. Suyver, a. Aebischer, S. García-Revilla, P. Gerner and H. U. Güdel, Phys. Rev. B - Condens. Matter Mater. Phys., 2005, 71, 1–9.
75 J. D. Kingsley, Appl. Phys. Lett., 1969, 15, 115.
76 Sommerdijk J. L., J. Lumin., 1971, 4, 441–449.
77 A. Pandey, V. K. Rai, R. Dey and K. Kumar, Mater. Chem. Phys., 2013, 139, 483–488.
78 H. W. Song, H. P. Xia, B. J. Sun, S. Z. Lu, Z. X. Liu and L. X. Yu, CHINESE Phys. Lett., 2006, 23, 474–477.
79 Y. Wang, L. Tu, J. Zhao and Y. Sun, J. Phys. Chem. C, 2009, 113, 7164–7169.
80 F. Liu, E. Ma, D. Chen, Y. Yu and Y. Wang, J. Phys. Chem. B, 2006, 110, 20843–20846.
81 J. Liao, L. Nie, S. Liu, B. Liu and H. Wen, J. Mater. Sci., 2014, 49, 6081–6086.
82 L. Lei, D. Chen, W. Zhu, J. Xu and Y. Wang, Chem. - An Asian J., 2014, 9, 2765–2770.
83 X. Bai, H. Song, G. Pan, Y. Lei, T. Wang, X. Ren, S. Lu, B. Dong, Q. Dai and L. Fan, J. Phys. Chem. C, 2007, 111, 13611–13617.
84 J. D. Suter, N. Pekas, M. T. Berry and P. S. May, J. Phys. Chem. C, 2014, 118, 13238–13247.
85 S. Wilhelm, M. Kaiser, C. Würth, J. Heiland, C. Carrillo-Carrion, V. Muhr, O. S. Wolfbeis, W. J. Parak, U. Resch-Genger and T. Hirsch, Nanoscale, 2015, 7, 1403–1410.

TOC-graphic:

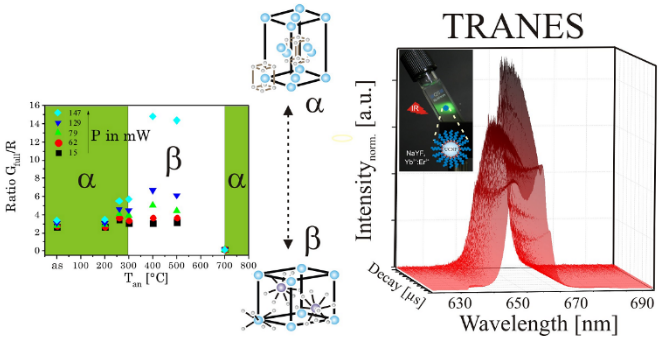
TRANES
Ratio G_{full}/R
T_{an} [°C]
as
100
200
300
400
500
600
700
800
0
2
4
6
8
10
12
14
16
147
129
79
62
15
P in mW
α
β
α
α
β
Intensity$_{norm.}$ [a.u.]
IR
NaYF$_4$ Yb^{3+}:Er^{3+}
UCNP
Decay [µs]
630
650
670
690
Wavelength [nm]